Journal of Analytical Science and Technology

RESEARCH ARTICLE Open Access

Study on the relationship between Bi_2S_3 with different morphologies and its photocatalytic hydrogen production performance

Xiaoyan Li[1,3], Lang Jun[3], Jiaxun Xiao[2], Yanqin Xu[1], Chuanyao Yang[2], Jinjing Tang[2], Kai Zhou[2], Xiangnan Gong[2*], Xiaoyuan Zhou[2*] and Hanjun Zou[2*]

Abstract

The morphology of a material is considered one of the primary aspects affecting its photocatalytic performance. Various methods have been developed to tailor the morphology of photocatalytic materials for photocatalytic water splitting. Bi_2S_3 is an excellent photoabsorption material with relatively narrow band gaps. Herein, Bi_2S_3 samples with different morphologies are successfully prepared via a simple one-step hydrothermal method and employed effectively as visible light-driven photocatalysts for hydrogen production. Electron microscopy technologies were used to characterize the morphology and microstructure of the Bi_2S_3 samples, which exhibit three kinds of morphologies, namely nanotubes, nanoflowers and nanorods. As a result, the Bi_2S_3 nanotubes have the largest BET specific surface area and lowest PL intensity, and these characteristics lead to having the best hydrogen production rate. Moreover, the catalysis mechanism is simply explained by studying the relationship between the morphology and microstructure of a material and its photocatalytic performance.

Keywords: Photocatalysis, Bi_2S_3 Nanotube, Hydrogen Production, Morphology

Introduction

Because of the energy shortage and the pressure of environmental protection, it is particularly important to develop new forms of energy other than fossil fuels. Photocatalytic hydrogen production has great potential because it is derived from natural sources such as water and solar energy, which are highly available, renewable and environmentally friendly (Suk et al. 2012; Qu et al. 2020). Since water splitting has been achieved on TiO_2 electrodes through a photoelectrochemical (PEC) approach to produce hydrogen, semiconductor technology for the photocatalytic decomposition of water has attracted the attention of many researchers (Fujishima and Honda 1972). Semiconductor catalysts play a vital role in the process of photocatalytic hydrogen production, both in the PEC reaction that was first discovered and the photochemical processes that followed (Liao et al. 2012). There are many factors affecting the performance of semiconductor photocatalysts, such as the band gap, structure and morphology, corrosion resistance, solution pH, and operating temperature (Ahmad et al. 2015; Chen et al. 2010; Maeda and Domen 2010). However, for the selection of photocatalytic materials, the band gap is the most critical factor because it determines the absorption and utilization efficiency of light energy. Unfortunately, traditional photocatalytic materials, such as TiO_2, ZnS and ZnO, are semiconductors that use only ultraviolet solar energy. Therefore, the

*Correspondence: xiangnan.gong@cqu.edu.cn; xiaoyuan2013@cqu.edu.cn; zhj8911@126.com

[2] Analytical and Testing Center, Chongqing University, Chongqing 401331, People's Republic of China
Full list of author information is available at the end of the article

development of photocatalytic materials with a wide spectral absorption range is of far-reaching significance to provide a breakthrough for photocatalytic hydrogen production applications (Liu et al. 2011; Chen et al. 2016; Ma et al. 2020).

Bi_2S_3 is a semiconductor with a relatively narrow band gap of 1.3–1.7 eV that can absorb visible light and even near-infrared light. It has been proven to be an excellent photoabsorption material widely used in photonic devices, such as photodetectors, solar cells, and all-optical diodes (Xu et al. 2012; Yu et al. 2019; Shan et al. 2019; Martinez et al. 2011). Its superwide light absorption range largely compensates for the shortcomings of TiO_2, WO_3, ZnS and other wide bandgap semiconductors as photocatalytic materials (Wang et al. 2017a; Kumar et al. 2016; Liu et al. 2021; Liu et al. 2016; Xiong et al. 2016). Sandeep Kumar et al. reported that TiO_2 nanoparticles were coupled with the Bi_2S_3 semiconductor to synthesize a heterostructure, which had a high visible light response. The results showed that the photocatalytic degradation efficiency of amaranth dye under solar light was much better than that of bare Bi_2S_3 and TiO_2 (Kumar et al. 2016). Zhu Liu et al. prepared a novel $Bi_2S_3/BiVO_4/TiO_2$ ternary heterostructure photocatalyst with a large light absorption coefficient. Compared with TiO_2 nanocrystals, the $Bi_2S_3/BiVO_4/TiO_2$ photocatalyst had a higher absorption intensity and extended the absorption range to near infrared. $Bi_2S_3/BiVO_4/TiO_2$ had a photocurrent of more than 10 times that of bare TiO_2 when performing photochemical experiments and had an approximately 4 times higher photocatalytic degradation efficiency than bare TiO_2 (Liu et al. 2021). Bi_2S_3/WO_3 thin films prepared by coating a layer of Bi_2S_3 on the surface of WO_3 nanoplate arrays exhibited higher PEC performance. The Bi_2S_3-modified WO_3 photoelectrode displayed a significantly higher photocurrent and higher electron transport rate due to the significant enhancement in response to visible light and good interfacial contact between the two crystals (Liu et al. 2016). A Bi_2S_3/ZnS composite was synthesized to obtain enhanced light absorption and a red-shifted absorption edge for more efficient separation of light-generated electron–hole pairs. The photocatalytic degradation performance of hexagonal Bi_2S_3/ZnS composites for methylene blue was better than that of pure Bi_2S_3 and pure ZnS, and the degradation rates were 7.1 times and 3.6 times higher than those of pure Bi_2S_3 and pure ZnS, respectively (Xiong et al. 2016).

Regarding materials with certain chemical compositions, a large number of studies have shown that the photocatalytic performance is closely related to the crystalline structure and morphology characteristics. Jiarui Li et al. reported that hexagonal $BiPO_4$, which has abundant phosphate defects, exhibited stronger photocatalytic activity than pure $BiPO_4$. DFT calculations revealed that defects induced the formation of intermediate energy levels within the band gap, allowing the effective charge to be transferred from the valence band to the conduction band (Li et al. 2019). The effects of morphology adjustment and defect engineering on the corresponding photocatalytic activity of $CaCu_3Ti_4O_{12}$-degrading antibiotics were systematically investigated by Reshalaiti Hailili, who revealed that the optimal photocatalytic performance was attributed to its unique morphology and effective carrier separation due to local defects (Hailili et al. 2019). Various methods have been developed to tailor the morphology of photocatalytic materials or to deposit photocatalytic materials on substrate materials with a unique morphology because the influence of morphology on the photocatalytic efficiency of materials is widely known (Hailili et al. 2019; Phan and Shin 2011; Wang et al. 2018; Farhadian et al. 2015). Different morphologies of TiO_2 materials have been used for the photocatalytic degradation of methylene blue. Among previously reported photocatalytic results, TiO_2 particles with prismatic and flower-like morphologies showed the highest photocatalytic activity, which was due to the synergistic effect between the morphology and crystal miscibility of TiO_2 (Phan and Shin 2011). The metal–organic framework compound ZIF-67 was synthesized with different morphologies for CO_2 reduction. The photocatalytic performance of ZIF-67 showed that the leaf shape of two-dimensional ZIF-67 has the best photocatalytic activity and stability, which was due to its highest adsorption capacity for CO_2 and effective electron transfer (Wang et al. 2018). WO_3 nanostructures with nanorod, nanosphere and nanoplate morphologies were prepared and characterized in this study to investigate the influence of shape on photocatalytic performance. The results show that WO_3 nanoplates have the best photocatalytic activity because of their lower coordination number, and the atoms located at the edges and corners of WO_3 nanoplates are more active (Farhadian et al. 2015).

However, there is very little literature on the influence of the structure and morphology of pure Bi_2S_3 crystals on photocatalytic performance. In this paper, Bi_2S_3 nanomaterials with nanotube, nanoflower and nanorod morphologies were synthesized by a hydrothermal method, and the influence of their crystallinity and morphology on their photocatalytic hydrogen production performance was studied.

Materials and methods

Preparation of Bi_2S_3 samples with different morphologies (Yao et al. 2009)

First, 1.226 g of $Bi(NO_3)_3{\cdot}5H_2O$ was dissolved in 5 mL of ethanol and stirred to form solution A. Second, 1.53 g of

$Na_2S{\cdot}9H_2O$ was dissolved in 10 mL of deionized water to form solution B. Third, 0.91 g of $CO(NH_2)_2$ was dissolved in 20 mL of deionized water to form solution C. Then, solution B was slowly added into solution A with magnetic stirring to form a black solution. Next, solution C was added to the black solution. The above solution was transferred to a 50 mL autoclave, and the autoclave was placed in an oven at 120 °C for 12 h at a constant temperature. The above solution was naturally cooled to room temperature, and a black precipitate was obtained by centrifugation. The solution was washed several times with ethanol to obtain Bi_2S_3 nanotubes.

Bi_2S_3 nanoflowers and nanorods were also synthesized through a similar synthesis method as that of Bi_2S_3 nanotubes, but the sulfur source of $Na_2S{\cdot}9H_2O$ was replaced by $Cs(NH_2)_2$ and $Na_2S_2SO_3$, respectively.

Material characterization

The crystal phase of the samples was determined via X-ray diffraction (XRD, PANalytical X' Pert Powder) using a Cu-Kα radiation source ($\lambda = 1.54186$ Å) in the 2θ range of 10–70° at a voltage and current of 40 kV and 40 mA, respectively. Raman analysis was characterized on a Raman spectrometer (LabRAM HR Evolution) using a solid-state laser with a wavelength of 532 nm as the excitation source. The morphology and structure of the samples were obtained by field-emission scanning electron microscopy (SEM, FEI Quattro S) and transmission electron microscopy (TEM, FEI Talos F200S). N_2 adsorption/desorption isotherms were analyzed with a specific surface and aperture analyzer (BELSORP-max-II) at 77 K to obtain the specific surface area and pore volume of the samples. The particle size of the samples was measured three times by dynamic light scattering (NanoBrook Omni, America). UV–vis diffuse reflectance spectroscopy (DRS) was performed with a UV–visible near-infrared spectrophotometer (Shimadzu, UV-3600) from 600 to 1200 nm with $BaSO_4$ as the reflectance standard to obtain the optical properties of the samples. Photoluminescence (PL) measurements were performed with a luminescence spectrophotometer (FLS1000) at an excitation wavelength of 335 nm. Time-resolved photoluminescence spectra (TRPL) were performed on a fluorescence spectrophotometer (FLS1000).

Photocatalytic performance evolution

The photocatalytic hydrogen evolution reaction was conducted in a glass container connected to a closed circulation and evacuation system (Beijing Perfect Light Company). The photocatalytic hydrogen production performance of the samples was evaluated under simulated sunlight irradiation with a 300 W Xe lamp. First, 0.5 M Na_2SO_3 and 0.5 M $Na_2S{\cdot}9H_2O$ were added as sacrificial agents to a glass container with 100 mL of deionized water; then, 20 mg of the catalyst was dispersed in the above solution. Next, the glass container with the above suspensions was degassed for 30 min under continuous and vigorous stirring to eliminate the gas and provide a vacuum environment for the reaction. The evolved H_2 of the samples was measured at 25 °C via gas chromatography (GC7900 Techcomp) with a thermal conductivity detector (TCD); Ar was used as the carrier gas.

Results and discussion

Structure and composition of Bi_2S_3 samples

To explore the crystal quality of Bi_2S_3 with different sulfur sources, the XRD patterns of the samples were analyzed, as shown in Fig. 1a. All the patterns of the samples exhibit sharp diffraction peaks, which indicate that all samples are highly crystalline. It can be seen that Bi_2S_3

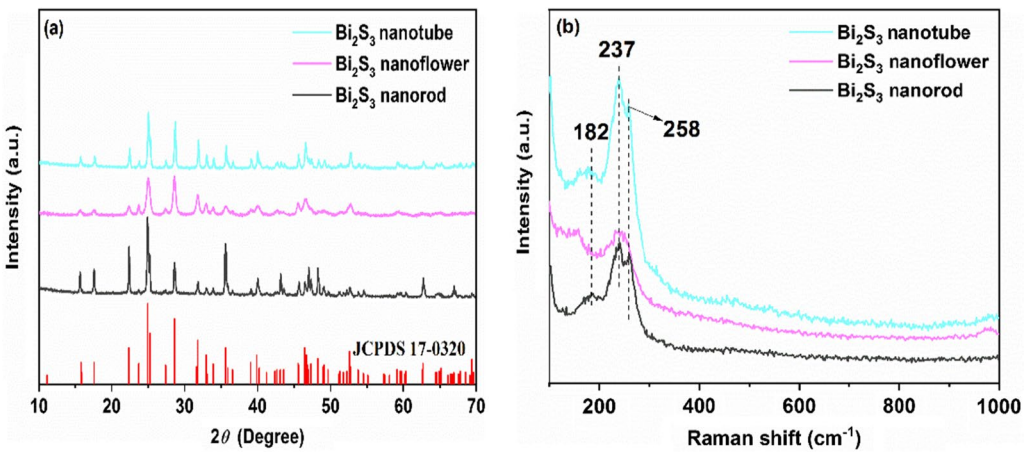

Fig. 1 **a** XRD patterns and **b** Raman spectra of Bi_2S_3 with different morphologies

exhibits orthorhombic crystal structure (JCPDS 17-0320) pattern, and no impurity peaks are detected, suggesting that all samples consist of a pure phase. Furthermore, the molecular structures of Bi_2S_3 were characterized by Raman spectroscopy, as shown in Fig. 1b. The peaks at 182, 237 and 258 cm^{-1} correspond to the Ag, Ag_1 and B1g modes of Bi_2S_3 with different morphologies, respectively (Wang et al. 2017b). These results clearly confirm that Bi_2S_3 samples with different morphologies are successfully achieved.

Morphological analysis of Bi_2S_3 samples

Bi_2S_3 prepared with different sulfur sources was characterized by SEM to reveal the variations in morphology and microstructure (Fig. 2a–f). The Bi_2S_3 nanotubes, based on the $Na_2S{\cdot}9H_2O$ sulfur source, are composed of a large number of linear products with a smooth surface and uniform diameters and lengths of 1–5 μm; additionally, these nanotubes are hollow with an outer diameter of 60–140 nm, an inner diameter of 10–48 nm and a tube wall of approximately 40 nm (Fig. 2a and b). The Bi_2S_3 nanoflowers, based on the $C_S(NH_2)_2$ sulfur source, are similar to three-dimensional spherical polymers with diameters of 2–7 μm; additionally, these nanoflowers are made up of many flat bands of microcrystals, growing in a divergent form from the center to all sides (Fig. 2c and d). The Bi_2S_3 nanorods, based on the $Na_2S_2SO_3$ sulfur source, have diameters of approximately 200 nm and lengths between 2 and 4 nm (Fig. 2e and f). TEM was then performed on the Bi_2S_3 nanotubes, and the results are shown in Fig. 3. The material has a hollow structure and a smooth surface with an internal aperture of approximately 50 nm and an outer diameter of less than 200 nm, further confirming that the material is a nanotube structure (Fig. 3a and b). Furthermore, the lattice spacing of the material is determined to be 0.398 nm and 0.197 nm, which can be assigned to the (220) plane and (002) plane of Bi_2S_3, respectively (Fig. 3c and d).

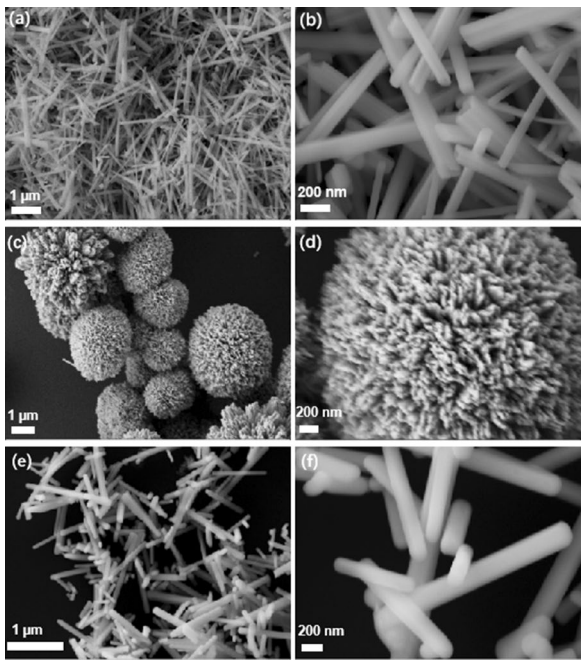

Fig. 2 SEM images of the **a**, **b** Bi_2S_3 nanotubes; **c**, **d** Bi_2S_3 nanoflowers; and **e**, **f** Bi_2S_3 nanorods

Surface area, pore structure and particle size of Bi_2S_3 samples

To identify the specific surface area and pore structure of the as-synthesized materials, N_2 adsorption–desorption isotherms were obtained for the Bi_2S_3 samples with different morphologies, as shown in Fig. 4. According to the IUPAC classification (Li et al. 2016), Bi_2S_3 nanotubes and Bi_2S_3 nanoflowers with a type IV isotherm represent a typical of mesoporous structures, while Bi_2S_3 nanorods with a type III isotherm show a nonporous structure. The specific surface area, pore size and pore volume analysis of the Bi_2S_3 samples are also presented in Table 1. The BET specific surface area of the Bi_2S_3 nanotubes is 14.5490 m^2/g, which is larger than those of the Bi_2S_3 nanoflowers (2.4578 m^2/g) and nanorods (7.9459 m^2/g). Simultaneously, the pore size distribution curve of three Bi_2S_3 samples is displayed in Fig. 4b. The pore size and pore volume are not available for Bi_2S_3 nanorods with a nonporous structure. Moreover, there is abnormal distribution curve for the pore size distribution of Bi_2S_3 nanotubes and Bi_2S_3 nanoflowers. Therefore, the average pore diameter is not relevant to the maximum value and middle pore size of the dV/dpW. Average pore size is usually used to describe the pore distribution of the sample. The average pore diameter and pore volume of Bi_2S_3 nanotubes (47.768 nm and 0.1596 cc/g) is larger than that of Bi_2S_3 nanoflowers (35.995 nm and 0.0345 cc/g). Due to the largest BET specific surface area, larger pore size and larger pore volume, Bi_2S_3 nanotubes do not only have more channels to facilitate the transmission of substances, but also provide more space for intermediate products. A larger specific surface area, larger average pore size and larger mesoporous volume provide many favorable advantages, including favoring the adsorption of water molecules, facilitating the transport of photogenerated carriers and providing more reactive active sites, thus promoting the photocatalytic performance of the material (He et al. 2021; Du et al. 2021; Wang et al. 2020). As mentioned above, the low PL intensity may correlate with the efficient charge transfer in the Bi_2S_3 nanotubes with the largest BET surface area, pore size and pore volume, thereby confirming the prevention

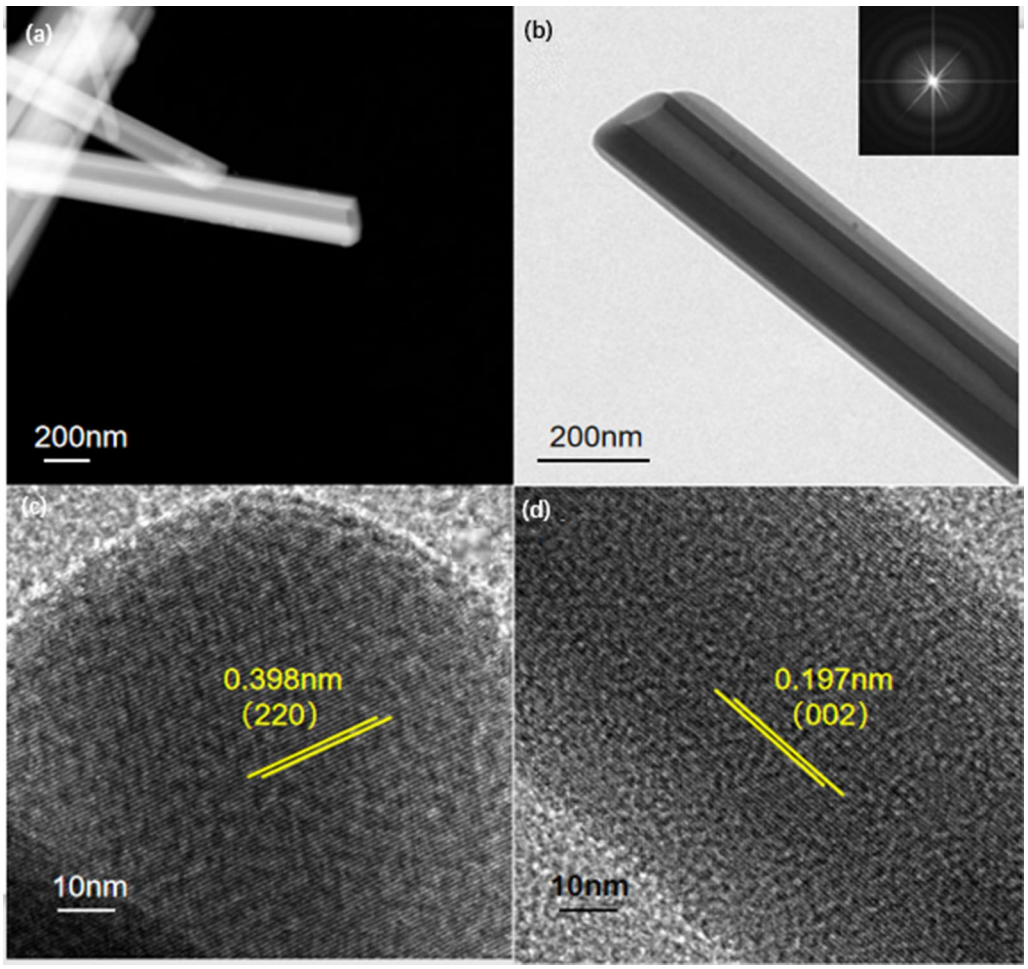

Fig. 3 **a**, **b** TEM images of the Bi_2S_3 nanotubes and **c**, **d** HRTEM images of the Bi_2S_3 nanotubes

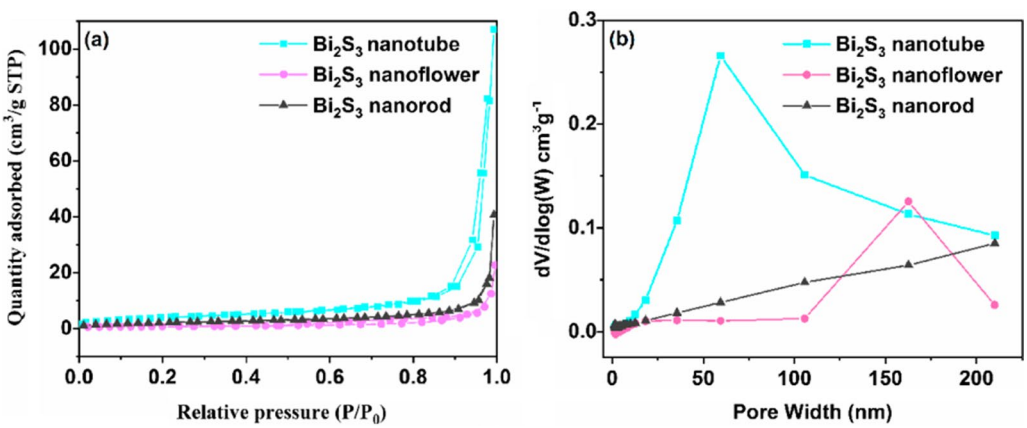

Fig. 4 **a** N_2 adsorption–desorption isotherms and **b** pore size distribution of the Bi_2S_3 samples with different morphologies

Table 1 Surface area, pore size and pore volume analysis of the Bi_2S_3 samples with different morphologies

Item category	Material		
	Bi_2S_3 nanotube	**Bi_2S_3 nanoflower**	**Bi_2S_3 nanorod**
Surface area (m^2/g)	14.5490	2.4578	7.9459
Average pore diameter (nm)	47.768	35.995	–
Middle pore size (nm)	53.212	59.476	–
Maximum pore size (nm)	120.21	162.71	–
Pore volume (cc/g)	0.1596	0.0345	–

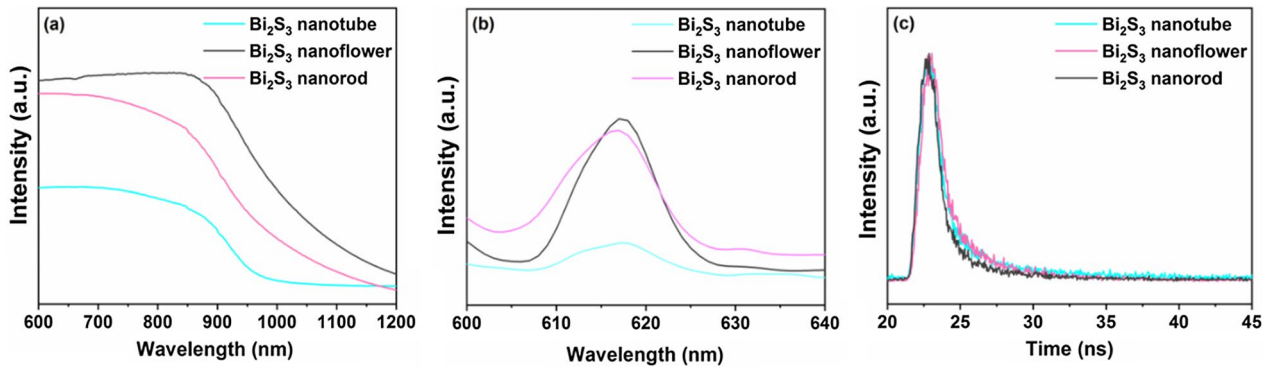

Fig. 5 **a** UV–vis DRS spectra, **b** photoluminescence spectra and **c** time-resolved fluorescence emission spectra of the Bi_2S_3 samples with different morphologies

of the direct recombination of electrons and holes. The particle size of the samples was measured by dynamic light scattering. The average particle size of Bi_2S_3 nanotubes (467 nm) is smaller than that of Bi_2S_3 nanoflowers (596 nm) and Bi_2S_3 nanorods (896 nm). It can be inferred that smaller size of Bi_2S_3 nanotubes is favorable for photocatalytic H_2 evolution.

Optical properties of Bi_2S_3 samples

The optical properties of the Bi_2S_3 catalysts with different morphologies are presented in Fig. 5. It is clearly shown that the as-prepared Bi_2S_3 has a good absorption region from the UV to infrared region; moreover, the Bi_2S_3 nanotubes demonstrate a distinct absorption band edge and no absorption after 1000 nm. In contrast, the edges of the absorption bands of the Bi_2S_3 nanoflowers and nanorods are not obvious (Fig. 5a). Furthermore, the PL intensity is positively correlated with the carrier combination rate. It is obvious that the PL emission intensity of the Bi_2S_3 nanotubes is lower than that of the Bi_2S_3 nanoflowers and nanorods (Fig. 5b). From the PL results, it can be deduced that the charge separation rate of Bi_2S_3 nanotubes is promoted under visible light irradiation. Simultaneously, TRPL spectra (Fig. 5c) were measured to demonstrate the charge carrier kinetics of Bi_2S_3 samples. As shown in Table 2, Bi_2S_3 nanotubes exhibit a longer average lifetime (3.0662 ns) than Bi_2S_3 nanoflowers (2.3734 ns) and Bi_2S_3 nanorods (2.1913 ns), indicating that charge separation efficiency is improved and the recombination of photoinduced electron–hole pairs is inhibited in the Bi_2S_3 nanotubes. These results reveal that more photoinduced electrons and holes at the interface of Bi_2S_3 nanotubes can contribute to a higher photocatalytic activity, as the charge recombination can be effectively inhibited.

Table 2 The PL lifetime parameters of the Bi_2S_3 samples with different morphologies

Material	Item category				
	τ_1 (ns)	**Rel (%)**	**τ_2 (ns)**	**Rel (%)**	**τ_{ave} (ns)**
Bi_2S_3 nanotube	0.8440	50.76	5.3468	49.24	3.0662
Bi_2S_3 nanoflower	0.8365	45.57	3.6601	54.43	2.3734
Bi_2S_3 nanorod	0.7938	62.54	4.5248	37.46	2.1913

Photocatalytic hydrogen production of Bi_2S_3 samples

The photocatalytic activity of the Bi_2S_3 samples was evaluated through the photocatalytic splitting of water

under simulated solar light irradiation. The time-dependent H_2 yields of the Bi_2S_3 samples with different morphologies are displayed in Fig. 6a and b. Clearly, compared with the Bi_2S_3 nanoflowers and nanorods, the Bi_2S_3 nanotubes with their hollow tubular structure exhibit the best rate of hydrogen production (271 μmol/h/g). In addition, it can be seen from Fig. 6c and d that the Bi_2S_3 samples with different morphologies can be maintained for four cycles with a total reaction time of 8 h, suggesting their good stability during the photocatalytic hydrogen production process. The photoreduction activity of a material depends on many factors. The first is a large BET specific surface area, which usually implies a large number of active sites on the surface. Bi_2S_3 nanotubes have both internal and external passages, thereby exhibiting a larger specific surface area that has more active sites for the photocatalytic hydrogen production reaction. A low PL intensity is another important factor that indicates the low recombination of charge carriers. The Bi_2S_3 nanotubes show the lowest PL intensity, which promotes electron–hole separation and migration. Therefore, it can be reasoned that Bi_2S_3 nanotubes, with more active sites and a lower recombination rate of electron–hole pairs, demonstrates higher photocatalytic performance.

To illustrate the photostability, the XRD pattern and SEM images of Bi_2S_3 nanotubes after photocatalytic H_2 production were further investigated. The XRD pattern of Bi_2S_3 nanotubes after photocatalytic H_2 production is presented in Fig. 6e. The morphology after photocatalytic H_2 production is also confirmed by SEM images. These results prove that Bi_2S_3 nanotubes exhibit good stability after photocatalytic H_2 production.

Conclusion

In summary, Bi_2S_3 samples with three morphologies are successfully designed for photocatalytic reactions by a facile hydrothermal method at 120 °C by changing the sulfur source. Compared with the Bi_2S_3 nanoflowers and nanorods, the Bi_2S_3 nanotubes exhibit the best hydrogen production performance and good stability. The above characterization analysis confirms that the improvement in performance of the Bi_2S_3 nanotubes possibly originates from the combined effect of their larger pore structure and wider reactive channels both inside and outside the Bi_2S_3 nanotube surface. This research may provide insight for the exploitation of photocatalytic hydrogen production and extend its application to other energy fields.

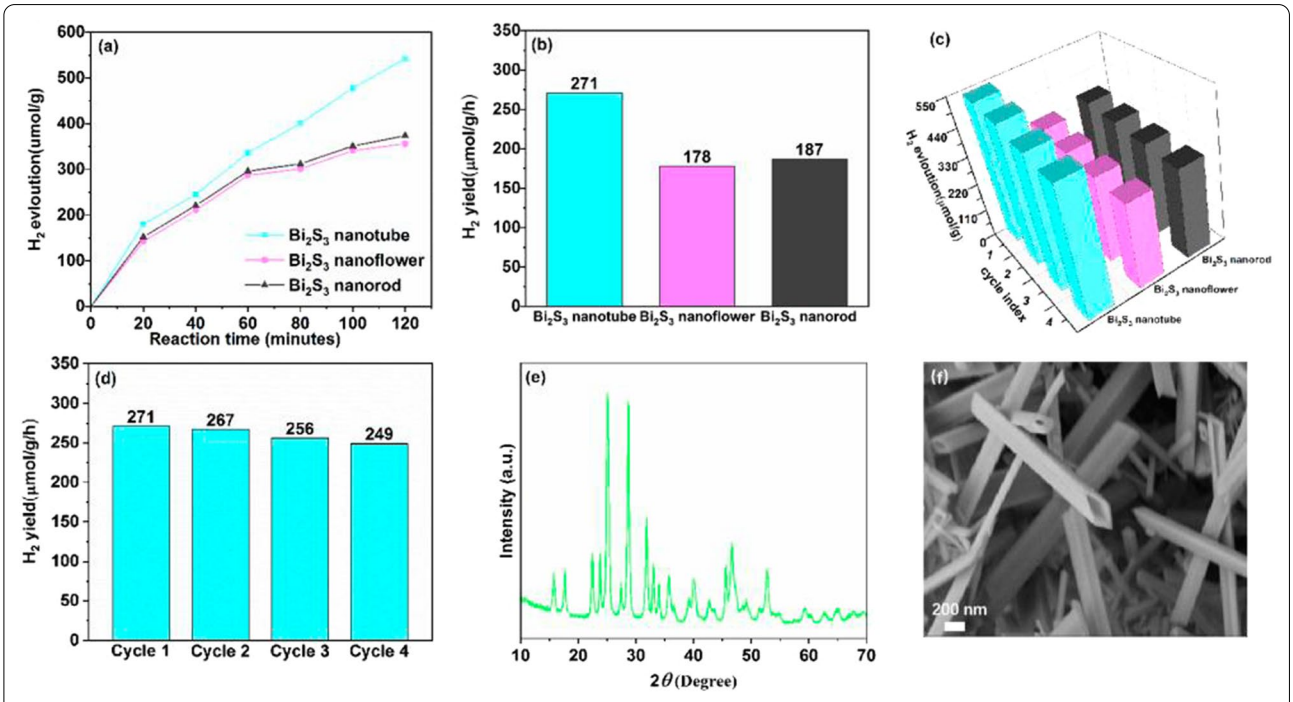

Fig. 6 **a** Photocatalytic H_2 evolution, **b** H_2 yield and **c** recycling test of the Bi_2S_3 nanotubes, nanoflowers and nanorods in a mixed aqueous solution containing Na_2SO_3 and Na_2S under simulated sunlight irradiation, **d** Four cycles of H_2 yield for the Bi_2S_3 nanotubes, **e** the XRD pattern and **f** SEM images of Bi_2S_3 nanotubes after photocatalytic H_2 production

Acknowledgements
We thank Analytical and Testing Center, Chongqing University, for providing us the necessary instrumentation facilities.

Author contributions
LJ carried out all the experiments mentioned in the manuscript. HJZ helped to draft the manuscript. XYL was the supervisor of the dissertation work. All authors read and approved the final manuscript.

Funding
This study was supported by the National Natural Science Foundation of China (NSFC51506018) and the Science and Technology Research Program of the Chongqing Municipal Education Commission (Grant No. KJQN201800707) for financial aid.

Availability of data and materials
Data sharing is not applicable. It will be shared if needed.

Declarations

Competing interests
The authors declare that they have no competing interests.

Author details
[1]School of Chemistry and Chemical Engineering, Chongqing University, Chongqing 401331, People's Republic of China. [2]Analytical and Testing Center, Chongqing University, Chongqing 401331, People's Republic of China. [3]Department of Materials Science and Engineering, Chongqing Jiaotong University, Chongqing 400074, People's Republic of China.

Received: 5 August 2021 Accepted: 6 May 2022
Published online: 07 June 2022

References

Ahmad H, Kamarudin SK, Minggu LJ, Kassim M. Hydrogen from photocatalytic water splitting process: a review. Renew Sust Energ Rev. 2015;43:599–610.
Chen XB, Shen SH, Guo LJ, Mao SS. Semiconductor-based photocatalytic hydrogen generation. Chem Rev. 2010;110(11):6503–70.
Chen XP, Zhang ZX, Chi L, Nair AK, Shangguan WF, Jiang Z. Recent advances in visible-light-driven photoelectrochemical water splitting: catalyst nanostructures and reaction systems. Nano-Micro Lett. 2016;8(1):1–12.
Du CY, Song JH, Tan SY, Yang L, Yu GL, Chen H, Zhou L, Zhang Z, Zhang Y, Su YH, Wen XF, Wang ST. Facile synthesis of Z-scheme ZnO/Ag/Ag_3PO_4 composite photocatalysts with enhanced performance for the degradation of ciprofloxacin. Mater Chem Phys. 2021;260: 124136.
Farhadian M, Sangpour P, Hosseinzadeh G. Morphology dependent photocatalytic activity of WO3 nanostructures. J Energy Chem. 2015;24(2):171.
Fujishima A, Honda K. Electrochemical photolysis of water at a semiconductor electrode. Nature. 1972;238(5358):37–8.
Hailili R, Yuan XX, Wang CY. A systematic investigation on morphology tailoring, defect tuning and visible-light photocatalytic functionality of Ti-based perovskite nanostructures. Catal Today. 2019;335:591–8.
He JY, Liu YL, Wang M, Wang YW, Long F. Ionic liquid-hydrothermal synthesis of Z-scheme BiOBr/Bi_2WO_6 heterojunction with enhanced photocatalytic activity. J Alloy Compd. 2021;865:158760.
Kumar S, Sharma S, Sood S, Umar A, Kansal SK. Bismuth sulfide (Bi_2S_3) nanotubes decorated TiO_2 nanoparticles heterojunction assembly for enhanced solar light driven photocatalytic activity. Ceram Int. 2016;42(15):17551–7.
Li ZD, Wang HL, Wei XN, Liu XY, Yang YF, Jiang WF. Preparation and photocatalytic performance of magnetic Fe_3O_4@TiO_2 core-shell microspheres supported by silica aerogels from industrial fly ash. J Alloy Compd. 2016;659:240–7.
Li JR, Zhang WD, Ran MX, Sun YJ, Huang HW, Dong F. Synergistic integration of Bi metal and phosphate defects on hexagonal and monoclinic $BiPO_4$: enhanced photocatalysis and reaction mechanism. Appl Catal b Environ. 2019;243:313–21.
Liao CH, Huang CW, Wu J. Hydrogen production from semiconductor-based photocatalysis via water splitting. Catalysts. 2012;2(4):490–516.
Liu ZW, Hou WB, Pavaskar P, Aykol M, Cronin SB. Plasmon resonant enhancement of photocatalytic water splitting under visible illumination. Nano Lett. 2011;11(3):1111–6.
Liu CJ, Yang YH, Li WZ, Li J, Li YM, Chen QY. In situ synthesis of Bi_2S_3 sensitized WO_3 nanoplate arrays with less interfacial defects and enhanced photoelectrochemical performance. Sci Rep. 2016;6:23451.
Liu Z, Xu K, Yu H, Zhang M, Sun ZQ. In-situ preparation of double Z-scheme Bi_2S_3/$BiVO_4$/TiO_2 ternary photocatalysts for enhanced photoelectrochemical and photocatalytic performance. Appl Surf Sci. 2021;545: 148986.
Ma YY, Jiang X, Sun RK, Yang JL, Jiang XL, Liu ZQ, Xie MZ, Xie EQ, Han WH. Z-scheme $Bi_2O_{23.3}$/Bi_2S_3 heterojunction nanostructures for photocatalytic overall water splitting. Chem Eng J. 2020;382:12302.
Maeda K, Domen K. Photocatalytic water Splitting: recent progressand future challenges. J Phys Chem Lett. 2010;1(18):2655–61.
Martinez L, Bernechea M, Arquer FPG, Konstantatos G. Near IR-sensitive, nontoxic, polymer/nanocrystal solar cells employing Bi2S3 as the electron acceptor. Adv Energy Mater. 2011;1(6):1029–35.
Phan TDN, Shin EW. Morphological effect of TiO_2 catalysts on photocatalytic degradationof methylene blue. J Ind Eng Chem. 2011;17(3):397–400.
Qu XF, Gao Z, Liu MH, Zhai HJ, Shi L, Li Y, Song HB. In-situ synthesis of Bi_2S_3 quantum dots for enhancing photodegradation of organic pollutants. Appl Surf Sci. 2020;501(31): 144047.
Shan YX, Li ZF, Ruan BX, Zhu JQ, Xiang YJ, Dai XY. Two-dimensional Bi_2S_3-based all-optical photonic devices with strong nonlinearity due to spatial self-phase modulation. Nanophotonics. 2019;8:2225–34.
Suk JJ, Gyu KH, Sung LJ. Heterojunction semiconductors: a strategy to develop efficient photocatalytic materials for visible light water splitting. Catal Today. 2012;185(1):270–7.
Wang RM, Cheng G, Dai Z, Ding J, Liu YL, Chen R. Onic liquid-employed synthesis of Bi_2E_3 (E = S, Se, and Te) hierarchitectures: the case of Bi_2S_3 with superior visible-light-driven Cr(VI) photoreduction capacity. Chem Eng J. 2017a;327:371.
Wang Y, Tian W, Chen L, Cao F, Guo J, Li L. Three-dimensional WO_3 nanoplate/Bi_2S_3 nanorod heterojunction as a highly efficient photoanode for improved pho-toelectrochemical water splitting. ACS Appl Mater Interfaces. 2017b;9(46):40235–43.
Wang M, Liu JX, Guo CM, Gao XS, Gong CH, Wang Y, Liu B, Li XX, Gurzadyan GG, Sun LC. Etal-organic frameworks (ZIF-67) as efficient cocatalysts for photocatalytic reduction of CO_2: the role of the morphology effect. J Mater Chem a. 2018;6(11):4768.
Wang K, Zhuo Y, Chen JY, Gao DW, Ren Y, Wang CX, Qi ZM. Crystalline phase regulation of anatase–rutile TiO_2 for the enhancement of photocatalytic activity. RSC Adv. 2020;10(71):43592–8.
Xiong DN, Huang GF, Zhou BX, Sl Chang, Wang F, Huang WQ. Enhanced photocatalytic activity of hexagonal flake-like Bi_2S_3/ZnS composites with a large percentage of reactive facets. J Phys D Appl Phys. 2016;49(30):305105.
Xu JZ, Li HN, Fang SF, Jiang K, Yao H, Fang F, Chen FM, Wang Y, Shi YM. Synthesis of bismuth sulfide nanobelts for high performance broadband photodetectors. J Mater Chem C. 2020;8(6):2102–8.
Yao GG, Ma H, Zhu GQ. Hydrothermal synthesisof Bi_2S_3 nanostructures with different morphologie. J Synth Cryst. 2009;38(6):1404–9.
Yu HZ, Wu ZP, Dong YF, Huang CW, Shi SW, Zhang YX. ZnO nanorod arrays modified with Bi_2S_3 nanoparticles as cathode forefficient polymer solar cells ZnO nanorod arrays modifiefficient polymer solar cells. Org Electron. 2019;75: 105369.

Publisher's Note